Orbital Angular Momentum based All-fiber Interferometer for Physiological Micro-movements Detection

Kang Yang*[a], Zefeng Ying[b], Huiyi Guo[c], Guoyu Li[d], Chao Wang[e], Lili Liang[a]

[a] Hebei Key Laboratory of Optical Fiber Biosensing and Communication Devices, Institute of Information Technology, Handan University, Handan 056005, China

[b.] Communication University of China, Beijing 100024, China

[c.] Institute of Modern Optics, Nankai University, Tianjin 300350, China

[d.] Handan Polytechnic College, Handan 056005, China

[e.] School of Engineering, University of Kent, Canterbury, CT2 7NT, United Kingdom

* Correspondence: yk@hdc.edu.cn; Tel.: +86-18603207958

Abstract:

An Orbital angular momentum (OAM)-based all-fiber interferometric sensing system is proposed for micro-scale mechanical displacements. A mode-selective coupler is employed to excite $LP_{11}^{\pm}$ modes, which can be further tuned to generate $OAM_{\pm1}$ states with phase fluctuations characterized by a standard deviation of 0.055 rad. The proposed system exhibits a linear response with a maximum sensitivity of 3.164 rad/μm and a minimum detectable displacement of 17.3 nm. Furthermore, physiological micro-movements are measured by placing the sensing arm on the radial artery or near the nostril. Repeated measurements demonstrate average relative errors of 3.145% for pulse rate and 1.345% for respiratory rate. The results confirm that the proposed OAM-based all-fiber interferometer offers an effective and non-invasive approach for high-resolution physiological signal detection, extending the application scope of OAM interferometric sensing in biomedical monitoring.

Keywords: Orbital angular momentum, Interferometric sensing, Physiological micro-movements, Optical fiber sensor

1. Introduction

Accurate monitoring of physiological micro-movements, such as arterial pulsation and respiration, provides valuable physiological information for health assessment and long-term vital-sign monitoring [1,2]. These physiological activities are generally accompanied by micrometer- to millimeter-scale mechanical displacements. To address such needs, sensing techniques with high sensitivity, excellent stability and immunity to electromagnetic interference are increasingly required.

Currently, the sensing techniques for physiological motion monitoring are generally classified into two categories: electrical wearable sensors and optical fiber-based sensors. Electrical sensing techniques mainly include three types: resistance sensors[3], electret capacitive sensors[4] and piezoelectric sensors[5， 6]. Although electrical sensors have low cost, high sampling frequency and circuit design flexibility. However, their performance may be affected by electromagnetic interference, baseline drift, motion artifacts and environmental variations during long-term monitoring[7]. Although fiber-optic sensors such as Fiber Bragg grating (FBG)[8], Fabry–Pérot (FP)[9], Polymer Optical Fiber POF[10], Distributed Optical

Fiber (DOF) [11] and micro-/nanofiber (MNF) [12] exhibit excellent sensitivity for physiological motion monitoring, many of these approaches rely on wavelength-, intensity-, or phase-demodulation schemes, which may increase system complexity and signal processing requirements. Therefore, alternative sensing mechanisms that can directly convert displacement-induced phase variations into easily measurable spatial features remain attractive for physiological monitoring applications.

Instead of conventional Gaussian-beam-based interferometers[13], a pair of conjugate orbital angular momentum (OAM) beams with opposite topological charges are employed as the test and reference beams, resulting in an interference pattern resembling a daisy flower, where the number of petals is twice the topological charge. OAM-based interferometers possess helical phase structures, enabling the mapping of phase variations into rotational changes of interference patterns. This unique phase-to-angle mapping mechanism offers considerable advantages for applications including contactless measurement [14], high resolution sensing [13,15], and accurate ranging measurements [16].

Most reported OAM interferometers adopt a bulk-optic free-space configuration, where a pair of conjugate OAM beams are typically generated using spatial light modulators (SLMs) [17] or spiral phase plates (SPPs) [14,18]. Although these approaches provide flexible OAM beam generation, they generally suffer from large physical size and poor compatibility with all-fiber systems, which limits their integration into compact sensing platforms. To address these challenges, fiber-based OAM interferometers offer a more compact architecture, high OAM mode conversion efficiency [19] and inherent compatibility with existing fiber systems. Compared with photon lanterns (PL) [20] and offset-splicing methods[21], mode selective couplers (MSCs) enable efficient excitation of degenerate LP_{11} modes with low insertion loss(insert loss less than 0.20 dB) [22] and high fabrication repeatability. By introducing a $\pi/2$ phase difference between the two degenerated LP_{11} modes, linearly polarized OAM modes can be generated efficiently.

In this work, an all-fiber OAM interferometer based on a home-made MSC [22]is proposed and experimentally demonstrated for physiological micro-movement detection. Petal-like interference patterns generated by the conjugated OAM beams with opposite topological charges have been applied for displacement sensing. The rotational variations correspond to phase changes induced by micro-scale displacements. Benefiting from the compact structure, low fusion loss, and inherent compatibility with fiber systems provided by the MSC, the proposed interferometer offers a practical and integrable sensing platform. As application demonstrations, physiological micro-movements induced by arterial pulsation and respiration are experimentally measured by placing the sensing arm in contact with the radial artery and near the nostril, respectively. Previous OAM interferometers were mainly demonstrated for static displacement or environmental sensing. The capability of OAM phase-to-rotation mapping for dynamic physiological micro-motion monitoring has rarely been investigated. These results extend the application scope of OAM interferometric sensing to physiological signal detection.

2. Principle

In a few-mode fiber, OAM modes can be obtained through the coherent superposition of two degenerated LP_{11} modes with a relative phase difference of $\pm\pi/2$. The two orthogonal LP_{11} modes can be expressed as:

$$\begin{aligned} LP_{11a} &= \mathrm{F}_{l,m}(r)\cos\varphi \\ LP_{11b} &= \mathrm{F}_{l,m}(r)\sin\varphi \end{aligned} \tag{1}$$

where $\mathrm{F}_{l,m}(r)$ and l represent the radial field distribution and the azimuthal order of OAM beams, respectively, φ is the azimuthal angle. By introducing a relative phase shift of $\pm\pi/2$ between the two degenerated modes, the resulting OAM modes can be written as:

$$\mathrm{OAM}_{+l,m} = LP_{11a} \pm iLP_{11b} \tag{2}$$

The resulting linearly polarized OAM modes can be represented using Jones vectors as [23]:

$$\begin{cases} \hat{\mathrm{x}}\mathrm{OAM}_{+l,m} = \begin{pmatrix} \mathrm{F}_{l,m}(r)\exp\,[il\varphi + i\alpha] \\ 0 \end{pmatrix} \\ \hat{\mathrm{x}}\mathrm{OAM}_{-l,m} = \begin{pmatrix} \mathrm{F}_{l,m}(r)\exp\,[-il\varphi - i\alpha] \\ 0 \end{pmatrix} \\ \hat{\mathrm{y}}\mathrm{OAM}_{+l,m} = \begin{pmatrix} 0 \\ \mathrm{F}_{l,m}(r)\exp\,[il\varphi + i\alpha] \end{pmatrix} \\ \hat{\mathrm{y}}\mathrm{OAM}_{-l,m} = \begin{pmatrix} 0 \\ \mathrm{F}_{l,m}(r)\exp\,[-il\varphi - i\alpha] \end{pmatrix} \end{cases} \tag{3}$$

Where α represents the phase change which caused by external disturbances, where the interference pattern rotates one period as α gradually increases from 0 to 2π. To verify the polarization state of the generated LP-OAM modes, the beam is analyzed using a polarizer [23].

Take the example with x-polarization, the interference pattern of the conjugated OAM beams with opposite topological charges can be expressed as below:

$$\begin{aligned} I(r,\varphi) &= \left|\mathrm{F}_{l,m}(r)\exp[il\varphi + i(\alpha_1)] + \mathrm{F}_{l,m}(r)\exp[-il\varphi - i(\alpha_2)]\right|^2 \\ &= \mathrm{F}_{l,m}^2(r)\{1 + \cos\,[2l\varphi - \Delta\alpha]\} \end{aligned} \tag{4}$$

Eq. (4) indicates that the interference pattern displays a petal-like structures with $2l$. For the case of $l = 1$, the interferogram shows two petals. When the optical path of the sensing arm changes, a phase shift $\Delta\alpha$ is introduced between the conjugated OAM beams with opposite topological charges, leading to an azimuthal rotation of the interference pattern. The phase shift induced by the axial change Δz can be described as follows:

$$\Delta\alpha = 2\pi\Delta\mathrm{z}/(\lambda) \tag{5}$$

Where λ represents the wavelength of the laser source. For the interference between the conjugated OAM beams, the rotation angle of the petal-like pattern $\Delta\beta$ is related to the phase shift by

$$\Delta\beta = \Delta\alpha/2l \tag{6}$$

Where l is the topological charge of OAM beam. By substituting Eq. (5) and Eq.(6), the relationship between the rotation angle of the interference pattern and the displacement can be obtained as:

$$\Delta\beta = \pi\Delta\mathrm{z}/(l\lambda) \tag{7}$$

This equation shows that the rotation angle of the interference pattern is proportional to the displacement applied to the sensing arm and inversely proportional to the topological charge of the OAM beam. It should be noted that the rotation angle $\Delta\beta$in Eq. (6) is expressed in radians. For experimental visualization and data processing, the measured rotation angles shown in physiological micro-movement detection are converted to degrees.

Fig. 1(a) shows the simulated interference patterns generated by the conjugated LP-OAM beams with different phase differences ranging from 0 to 2π. The phase difference between the two beams is varied from 0 to 2π in increments of 15°, as indicated at the top of each subplot. As the phase difference increases, the petal-like pattern rotates continuously in the azimuthal direction. Fig. 1(b) illustrates the relationship between the readable rotation angle and the accumulated total rotation angle. When the rotation angle (readable angle) continuously increases or decreases beyond one cycle, the measured actual rotation angle (total angle) should correspondingly increase or decrease by one cycle (360°). Thus, the range of the readable angle should be between 0° and 360°. The total rotation angle increases linearly with the phase difference.

According to Eq. (7), the rotation angle is inversely proportional to the topological charge l. A larger l leads to a smaller rotation angle under the same displacement, which reduces the measurement resolution. Therefore, in this work, LP-OAM beams with a topological charge of $l = 1$ were selected to achieve higher displacement sensitivity.

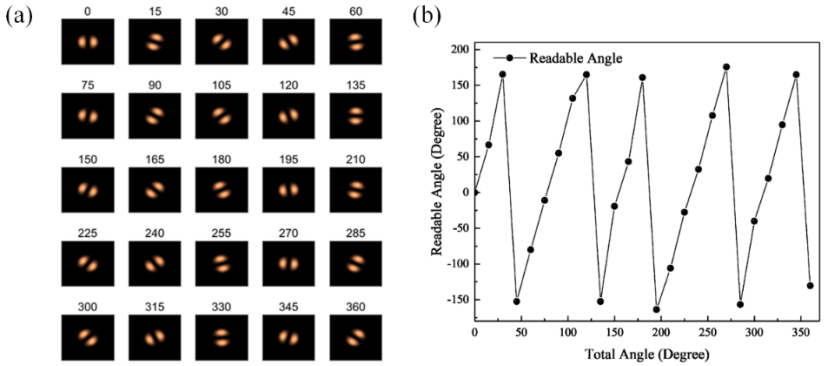


Fig.1 Simulation results of (a) the interference patterns generated by LP-OAM±1 beams as a function of phase difference (b) The relationship between the readable angle and the total angle.

3. Experimental Setup

An all-fiber interferometer based on MSC is constructed to realize axial micro-displacement measurements in fiber. The experimental setup of the proposed OAM interferometer is shown in Fig.2. A tunable laser operating at a wavelength of 1550 nm with an output power of 18 mW is used as the light source. The laboratory temperature is maintained at 20 °C during the experiment.

The in-house fabricated MSC is employed to convert the fundamental mode into the LP_{11} mode. Polarization controller (PC1) placed along the fiber path is used to adjust the splitting ratio of the two subsequent LP modes (LP_{11}^{a} and $LP\ _{11}^{b}$). PC2 and PC3 are adjusted to ensure the correct generation and manipulation of LP-OAM modes ($\hat{x}OAM_{+1}$ or $\hat{x}OAM_{-1}$).

Two collimators (Col. 1 and Col. 2) are used to collimate the output beams from the fiber arms. A beam splitter (BS) combines the two OAM beams into one optical path to generate the interference pattern used for displacement sensing. The OAM beam in the upper branch is reflected once by the BS, resulting in an opposite topological charge compared with the beam in the lower branch. A CCD camera is employed to capture the interference patterns produced by the conjugated OAM beams for further analysis.

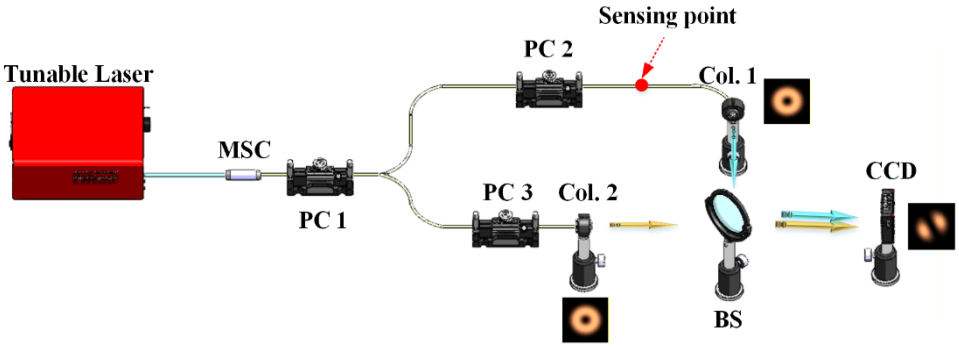


Fig. 2. Experimental setup of the all-fiber OAM interferometer. MSC: mode-selective coupler; PC: polarization controller; Col.: collimator; BS: beam splitter; CCD: charge-coupled device.

To verify the interference mechanism, the output mode patterns of the two interferometer arms are analyzed. Fig.3(a) presents the experimental and simulated optical field distributions of first-order LP-OAM beams after passing through a polarizer. Each row contain shows experimental (Exp.) and simulated (Sim.) results corresponding to different angles between the polarizer and the optical axis (0°, 45°, 90°, and 135°). When $\theta = 0°$, the optical field displays

a ring-shaped intensity distribution. As the polarizer rotates to $\theta = 90°$, the intensity distribution becomes significantly suppressed. The observed variations agree well with the theoretical predictions described by Eq. (6), it can be determined that both arms of the interferometer generate the expected LP-OAM modes.

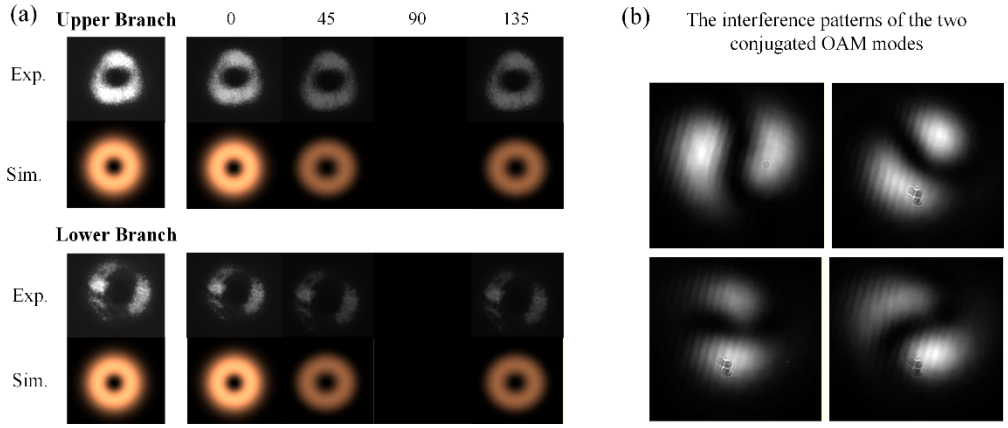


Fig.3 (a) Experimental and simulation mode patterns of the output beams from the two interferometer arms. (b) interference patterns generated by the superposition of conjugated OAM beams with different initial phase differences.

Fig.3(b) shows the petal-like interference patterns generated by the superposition of the conjugated OAM beams with opposite topological charges. Based on Eq. (6), the rotated angles of the interference pattern is related to the relative phase difference between the two interferometer arms. The rotation angle is calculated by detecting the centroids of two bright spots in each captured image. The slope between these centroids is then determined and converted into an angular value using the arctangent function. This method enables efficient angle extraction with minimal computational complexity, allowing rapid processing of the captured interference patterns.

4. Axial displacement measurement based on rotation angle demodulation

Based on the LP-OAM interferometer, the axial displacement Δz in Eq. (5) is applied by controlling axial movements along the sensing fiber, which results in the rotation of the interference pattern. Therefore, the proposed system enables quantitative measurement of axial displacement through rotation angle demodulation.

The stability of the interference pattern is obtained by recording the rotation angle over a period of 2 minutes without applying any external perturbation. As shown in Fig.4, the fluctuations exhibit a standard deviation of 0.055 rad. The measurements are performed at a frame rate of 14 frames per second. The observed fluctuations are mainly attributed to minor environmental disturbances, including temperature variations in the laboratory, mechanical vibrations of the experimental platform, and air flow.

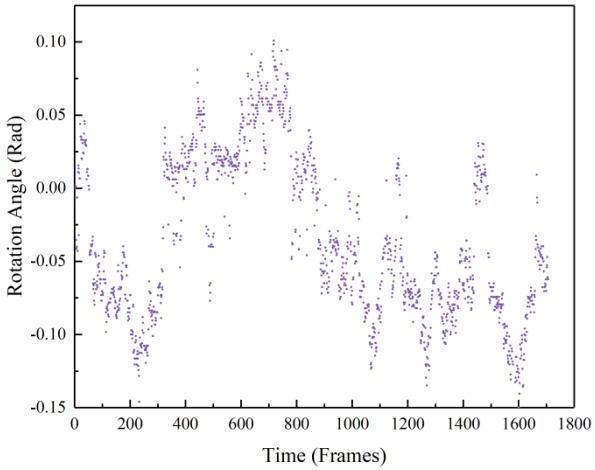


Fig.4 The noise analysis of the interference pattern over a 2-minute period without external perturbations.

Fig.5 presents the sensor response curves for bidirectional axial displacement measurements. The inset illustrates the experimental setup corresponding to sensing position in Fig. 2. The few-mode fiber is fixed on two one-dimensional translation stages using holder. The left end is kept fixed, while the right end is stretched by adjusting the translation stage in steps of 10 μm.

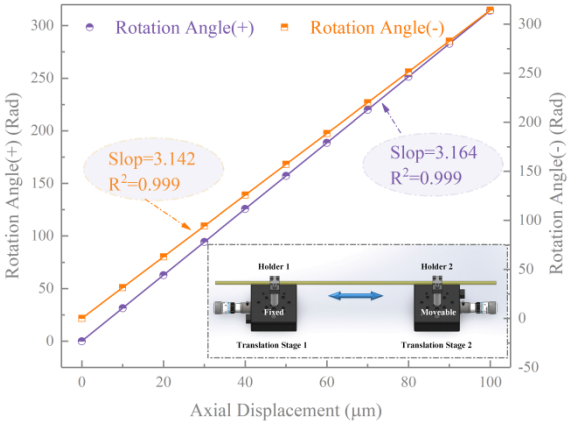


Fig.5 The rotation angles versus the applied axial movements and the linear fitting line in bidirectional

The orange and purple curves represent the sensor responses during increasing and decreasing axial displacement, respectively. The corresponding sensitivities are measure to be 3.142 rad/μm and 3.164 rad/μm, demonstrating good agreement and clear linear relationship between the rotation angle and the applied displacement, as indicated by the fitted lines in Fig. 8.

Based on the fluctuation of the rotation angle with a standard deviation of 0.055 rad, the minimum detectable displacement is estimated to be 17.3 nm, indicating high detection resolution. These results demonstrate that the proposed interferometer can effectively convert axial displacement into measurable rotation angle variations, enabling quantitative characterization of micro-scale displacements.

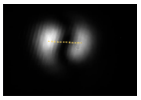
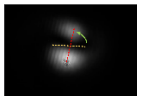
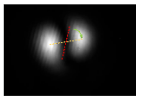
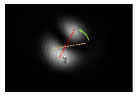
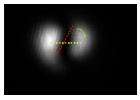
5. Physiological Micro-movement detection

Based on the quantitative relationship established between axial displacement and rotation angle in the previous section, the proposed OAM interferometer was further applied to physiological micro-movement detection.

Physiological activities, including pulse and respiration, introduce periodic perturbations to the sensing arm, resulting in alternating forward and reverse rotations of the OAM interference pattern. One complete cycle of forward and reverse rotation corresponds to a full physiological cycle. To quantitatively characterize these periodic signals, the maximum rotation angles during the forward and reverse rotations within each cycle were selected as characteristic parameters. Previous biomedical studies have demonstrated that radial artery pulsation and respiration-induced airflow around the nostril can generate periodic mechanical disturbances on the skin and surrounding tissues [24–26]. These physiological motions provide the mechanical stimuli detected by the proposed sensing system and are converted into optical phase variations according to the phase-to-rotation mapping mechanism described in Eq. (7).

To illustrate the angle extraction process, Table 1 presents a representative pulse measurement (69 bpm), showing the variation of the interference-pattern rotation angle over two physiological cycles. The extracted rotation angles exhibit periodic bidirectional variations corresponding to the cyclic mechanical perturbations transferred to the sensing fiber. These results verify that the proposed system can effectively resolve physiological micro-movements through the rotation of the OAM interference pattern.

Table 1 interference pattern rotation angles in two pulse cycles

Time (s)	0	0.43	1.16	1.96	2.2
Rotation Angle (Deg)	0	-81.63	78.57	-74.6	78.57
Interference Pattern Snapshots					

Based on this principle, physiological signals were further reconstructed from the extracted rotation-angle sequences. As shown in Fig. 6, the sensing arm was positioned at the wrist and near the nostril for pulse and respiration measurements, respectively.

Figure 6(a) presents a representative pulse measurement result. A clear periodic waveform can be observed in the demodulated signal, and the corresponding frequency spectrum exhibits a dominant peak at 1.15 Hz, corresponding to a pulse rate of 69 bpm.

Similarly, Fig. 6(b) shows the respiration measurement result. The extracted signal exhibits a lower-frequency periodic variation, and the corresponding frequency spectrum shows a dominant peak at 0.36 Hz, corresponding to a respiration rate of 22 breaths/min.

The results demonstrate that the periodic physiological perturbations can be successfully converted into rotation-angle variations and subsequently demodulated to obtain pulse and respiration rates.

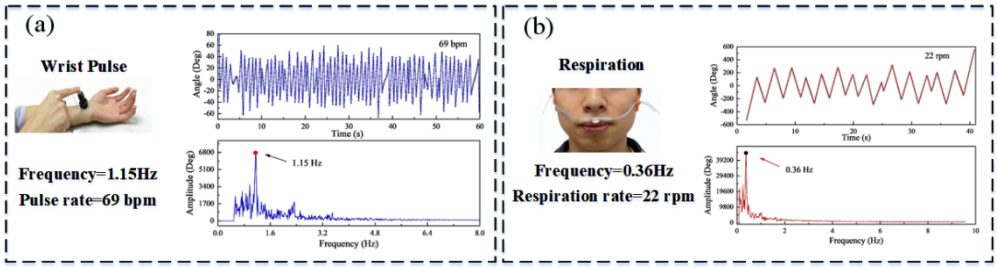


Fig. 6 Physiological micro-movement detection (a) pulse rate measurement results (pulse rate=69 bpm); (b) respiration measurement results (respiration rate=22 rpm)

Based on the measured maximum accumulated rotation angles in Fig. 6 and Eq. (7), the corresponding effective displacements acting on the sensing fiber are estimated to be on the order of several tens of micrometers. These values are consistent with the expected displacement transfer from physiological motion to the sensing fiber through tissue deformation or airflow-induced perturbations.

To further evaluate the reliability of the proposed sensing system, repeated measurements were conducted for both pulse and respiration signals. The pulse rate and respiration rate were each measured ten times under different physiological conditions, and the results are summarized in Table 2. For respiration measurements, the reference rates ranged from 10 to 38 breaths/min. Compared with commercial instrument (Medisana MD300CI216R), the measurement errors were within 0–1 breaths/min, corresponding to a maximum relative error of 4.34% and an average relative error of 1.345%. For pulse measurements, the reference rates ranged from 40 to 120 beats/min. The measurement errors were within 0–7 beats/min, corresponding to a maximum relative error of 6.15% and an average relative error of 3.145%.

Overall, the proposed sensing system achieved reliable physiological-signal detection with average relative errors below 4% for both pulse and respiration measurements.

Table 2 Measurement Results of Respiratory rate and Pulse rate over ten times

	Actual Value (MD300CI216R)	Calculated Value (OAM based Interferometer)	Absolute Error	Relative Value	Average Relative Error
Respiratory rate	10	10	0	0	1.345%
	11	11	0	0	
	13	13	0	0	
	14	14	0	0	
	15	15	0	0	
	21	21	0	0	
	23	22	1	4.34%	
	29	30	1	3.45%	
	33	32	1	3.03%	
	38	37	1	2.63%	
Pulse rate	40	41	1	2.5%	3.145%
	54	54	0	0	
	58	60	2	3.44%	
	59	61	2	3.38%	
	61	62	1	1.63%	
	65	69	4	6.15%	
	69	65	4	5.79%	
	71	71	0	0	
	73	75	2	2.73%	
	120	113	7	5.83%	

The slightly larger errors observed in pulse measurements are mainly attributed to the higher signal frequency and smaller rotation-angle variations compared with respiration signals. Under these conditions, the centroid-based angle extraction algorithm becomes more susceptible to image noise and interference-pattern fluctuations, leading to increased uncertainty in frequency estimation. Nevertheless, the obtained results confirm that the proposed OAM interferometer can accurately resolve both pulse and respiration signals and provides a promising platform for non-invasive physiological monitoring.

6. Conclusions

In this work, an OAM-based all-fiber interferometric sensing system is proposed for micro-displacement detection by converting phase variations into measurable rotation angles of interference patterns. By employing a mode-selective coupler, LP-OAM modes are generated in a compact and fiber-compatible configuration. The system achieves a displacement sensitivity of up to 3.164 rad/μm, exhibiting a nearly linear relationship between the rotation angle and the applied axial displacement. This method is further validated through physiological micro-movement measurements, where pulse and respiration signals are successfully extracted. Statistical analysis over repeated trials shows that the relative errors remain below 3.145% for pulse rate measurements and 1.345% for respiratory rate measurements.

The proposed approach provides a compact and effective solution for converting micro-scale mechanical motion into optical rotational signals, offering a new perspective for OAM-based fiber sensing. It shows promising potential for applications requiring non-invasive and high-resolution motion detection.

Funding. This work was supported by Hebei Provincial Higher Education Scientific Research Project (No. ZC2025020); the Natural Science Foundation of Hebei Province [grant number F2024109002]; the Hebei Key Laboratory of Optical Fiber Biosensing and Communication Devices [grant number SZX2022010]; the Science and Technology Project of Hebei Education Department [grant number CXZX2026021];

References

[1] J Xu, Y Hao, T Li, L Huang, L Niu, C Zhang, et al. A wearable sensor with environmental robustness based on tapered optical fiber coupling for respiration monitoring[J]. Optics & Laser Technology, 195(2026) 114555, https://doi.org/10.1016/j.optlastec.2025.114555.

[2] J Li, H Li, Z Long, et al. Wearable multifunctional optical sensor based on Er3+/Yb3+ co-doped Gd2O3 nanoparticles and tapered U-shaped fiber[J]. Optics Letters, 50(2025):281-284, https://doi.org/10.1364/OL.544678.

[3] X Li, Y Li, H Wei, et al. A Review of Wearable Optical Fiber Sensors for Rehabilitation Monitoring[J]. Sensors, 24(2024) 3602, https://doi.org/10.3390/s24113602.

[4] S A Zawawi, A A Hamzah, B Y Majlis, et al. A Review of MEMS Capacitive Microphones[J]. Micromachines, 11(2020) 484, https://doi:10.3390/mi11050484.

[5] Y Torabi, S Shirani, J P Reilly, G M Gauvreau. MEMS and ECM Sensor Technologies for Cardiorespiratory Sound Monitoring—A Comprehensive Review[J]. Sensors, 24(2024)7036, https://doi.org/10.3390/s24217036.

[6] Y Yang, B Wang, J Cui, et al. Design and Realization of MEMS Heart Sound Sensor with Concave, Racket-Shaped Cilium[J]. biosensors, 12(2022)534, https://doi.org/10.3390/bios12070534.

[7] K Chen, Y Guo, X Sun. Intelligent fiber optic integrated sensing system for human motion monitoring[J], Optical Fiber Technology, 81(2023)103535, https://doi.org/10.1016/j.yofte.2023.103535.

[8] S Koyama, Y Sato, H Maru, et al. Wearable FBG Sensor System for Respiratory Strain Measurement During Daily Activities[J]. IEEE Sensors Journal, 24(2024) 20595-20605, https://doi.org/10.1109/jsen.2024.3396784.

[9] H Liu, S Wang, J Jiang, et al. Pressure-insensitive low-density polyethylene diaphragm-based optical fiber temperature sensors[J]. Optics Express, 33(2025) 14537-14543, https://doi.org/10.1364/OE.559765.

[10] Q Q Ge, T Zhou, T Y Gong, et al. Highly sensitive measurement of finger joint angle based on a double-U tapered POF embedded in PDMS film[J]. Optical Fiber Technology, 76(2023)103236, https://doi.org/10.1016/j.yofte.2023.103236.

[11] R Jin, C He, C Li, et al. Positioning Error Limits and Noise Analysis in Hybrid MZ-Sagnac Interferometric Distributed Optical Fiber Sensing System[J]. Journal of Lightwave Technology, 43(2025) 2438-2448, https://doi.org/10.1109/JLT.2024.3486815

[12] J Fan, H Liang, Y Sun, et al. A high-sensitivity optical fiber temperature sensor based on PDMS microcavity combining Fabry–Pérot interferometer (FPI) and Mach–Zehnder interferometer (MZI)[J]. Measurement, 259(2026) 119626, https://doi.org/10.1016/j.measurement.2025.119626.
[13] Z Dai, L Lai, Y Liang, et al, Design of a magnetic field and temperature fiber sensor based on Fabry–P´erot interferometer and OAM interrogation[J], Optics Communications, 554(2024) 130166, https://doi.org/10.1016/j.optcom.2023.130166.
[14] J Zhu, F Han, L Wang, et al. Fractional Orbital Angular Momentum Sensor for Dynamic Micro-Displacement[J]. Journal of Lightwave Technology, 42(2024) 1689-1695, https://doi.org/10.1109/JLT.2023.3322706.
[15] L Gy, J Chen, H Guo, Z Wang, Y Liu. High-precision and alignment free all-fiber optical vortex interferometer[J]. Photonics Research, 1(2026):256-266.
[16] A E Willner, Y Duan, Z Jiang, et al, Optical ranging through turbid underwater media using spatially structured beams[J], APL Photonics, 10(2025) 090803, https://doi.org/10.1063/5.0268347.
[17] X Fan, X Wu, L Zhou, et al, Configurable optical vortex ladder in free space[J]. APL Photonics, 10(2025) 036107, https://doi.org/10.1063/5.0248825.
[18] D Yang, Z Yang, Y Zhang. Wavefront-splitting interferometer based on orbital angular momentum beams[J]. Optics Express, 31(2023) 28955, https://doi.org/10.1364/OE.498081.
[19]F Ren, Y Mao, Q Xu, et al, Stable and selectable generation of LP/CVB/OAM modes in an all-fiber ring laser via a low modal-crosstalk mode multiplexer/demultiplexer[J], Optics Express, 33(2025) 39373-39395, https://doi.org/10.1364/OE.569662.
[20] L Chen, H Guo, Z Shi, et al. Single-Fiber-Derived High-Order Mode-Group Selective Photonic Lantern[J], Journal of Lightwave Technology, 43(2025) 6873-6878, https://doi.org/10.1109/JLT.2025.3559327.
[21] X Liu, R Singh, M Li, et al. Plasmonic sensor based on offset-splicing and waist-expanded taper using multicore fiber for detection of Aflatoxins B1 in critical sectors[J]. Optics Express, 31(2023) 4783-4802, https://doi.org/10.1364/OE.479870.
[22] H Guo, L Chen, Z Shi, et al. Ultra-low-loss 5-LP mode selective coupler based on fused biconical taper technique [J]. Optics express, 31(2023) 18050-18062, https://doi.org/10.1364/OE.491818
[23] B Mao, Y Liu, H Zhang, et al. Complex analysis between CV modes and OAM modes in fiber systems[J]. Nanophotonics, 8(2018), https://doi.org/10.1515/nanoph-2018-0179.
[24] Xinxing Shao, Xiangjun Dai, Zhenning Chen, and Xiaoyuan He, "Real-time 3D digital image correlation method and its application in human pulse monitoring," Appl. Opt. 55, 696-704 (2016).
[25] Xue Yuan, Su Yong, Zhang Chi, et al. Full-field wrist pulse signal acquisition and analysis by 3D Digital Image Correlation [J]. Optics and lasers in engineering, 98(2017):76-82.
[26] Zefeng Hou, Jianzhang Liu, Yifei Liao, et al. Design and application of flexible wearable sensors based on optical fibers[J]. Talanta, 297(2026):128576.